Nanoscale Advances

Accepted Manuscript

This article can be cited before page numbers have been issued, to do this please use: S. K. Pardeshi, A. P. Alegaonkar and P. Alegaonkar, *Nanoscale Adv.*, 2020, DOI: 10.1039/D0NA00021C.

ROYAL SOCIETY OF CHEMISTRY

rsc.li/nanoscale-advances

View Article Online
DOI: 10.1039/D0NA00021C

Electrochemical performance of self-assembled two-dimensional heterostructure of rGO/MoS_2/h-BN

Ashwini P. Alegaonkar [a], Prashant S. Alegaonkar [b, 1], Satish K. Pardeshi [a, **]

[a] *Department of Chemistry, Savitribai Phule Pune University (Formerly University of Pune), Ganeshkhind, Pune 411 007, MS, India*

[b] *Department of Physics, School of Basic and Applied Sciences, Central University of Punjab, City Campus, Mansa Road, Bathinda 151 001, Punjab, India*

Abstract

We report on preparation and electrochemical performance evaluation of two dimensional (2D) self-assembled heterostructure of graphene oxide (rGO), Molybdenum disulphide (MoS_2), and hexagonal boron nitride (h-BN). In present study, rGO-MoS_2-h-BN (GMH) multi-layered GMH heterostructure is fabricated by in-situ route chemical technique. In material analysis, the composite consists of bond conformation of C-B-C, Mo-S, C-N, B-N, Mo-C indicating layered stacks of rGO/h-BN/MoS_2. In electrochemical analysis, composite performed superior in aqueous medium of cobalt sulphate ($CoSO_4$) over others. CV measurements, carried out over 10-100 mVs^{-1}, showed change in specific capacitance (C_{sp}) from 800 to 100 Fg^{-1}. GMH hardly showed any degradation up to 20,000 cycles @100mVs^{-1}. The calculated C_{sp}, energy-(E_D), power-(P_D) density has been discussed in light of Nyquist, Bode, and Ragone analysis. Equivalent circuit is simulated for cell and discussed for its discrete electronic components. Due to larger effective electron diffusion length >1000µm, broadly, composite showed *battery-like* characteristic, as supported by radical paramagnetic resonance and transport response. The symmetric electrodes prepared in one step, are facile to fabricate, easy to integrate and involved no pre or post treatment. They possess superior *flat cell* character, cost effective, and favourable towards practicality at an industrial scale, as demonstrated on the laboratory bench. The details are presented.

Keywords : 2D materials, electrochemical performance, battery-like behaviour, limiting capacitance, renewable energy

[1] Co-corresponding author (P. S. Alegaonkar) mail: prashant.alegaonkar@gmail.com
**Corresponding author (S.K. Pardeshi) mail: skpar@chem.unipune.ac.in

View Article Online
DOI: 10.1039/D0NA00021C

1. Introduction:

Today's industrial market need compact instruments with high energy storage devices and the demand is ever-increasing for such type of power backups. The widespread usage of Lithium–ion battery technology is mainly due to advances in its technology. The rechargeable lithium-ion batteries have already acquired *mile-stone* position as dominant energy sources powering almost all forms of consumer electronics including electric vehicles strategic system, digital home appliances etc. Due to its capability to provide high energy density (E_D). In spite of its extensive use it has several drawbacks in the form of poor cycle life, low power performance, fire hazards and carcinogenic waste aging effect, expensive. [1] In recent years supercapacitors are considered as alternative choice due to their safety aspects, packed with capability to deliver ~10 times more power density (P_D) than batteries, and everlasting millions of charge/discharge cycles. [2-3] Further Today's batteries not sufficient to enable car driving distances comparable to those of combustion energy-driven vehicles. In order to commercially realise the technology of supercapacitors enormous amount of research endeavour, to improvise technical specifications, like E_D, P_D, life cycle, etc. A considerable amount of work has been carried out to fabricate electrode material, electrolyte environment selection etc. Several two-dimensional (2D) material such as graphene, molybdenum disulphide, hexagonal boron nitride, transition metal dichalcogenides (TMDCs), *g*-C_3N_4, phosphorene layered double hydroxides and MXenes [4-8] desirable for energy storage application due to their outstanding structural-property relationship. Besides graphene, transition metal dichalcogenides (TMD), post graphene contenders, transition metal oxides (TMO) /hydroxides (TMH) are considered as a potential candidate. The structures of TMO and TMH in the form of films, flakes, platelets, petals, belts, etc., significantly alters the inherent properties of supercapacitors showing excellent E_D. This is a huge class among which, we have specifically chosen reduced graphene oxide (rGO), MoS_2 and h-BN in the form of blend to investigate their electrochemical performance. Basically, the use of carbon compounds in energy storage devices have its own advantages in the form of superior performance characteristic, high surface area, low cost, affordability to large scale applications and easy preparation protocols. There are number of reports on use of nanocarbons such as rGO, single walled- carbon nanotube (CNTs), CNTs/Polymer, rGO-TMO, activated carbon, multi walled-CNTs to achieve superior specific

View Article Online
DOI: 10.1039/D0NA00021C

capacitance ($C_{sp,}$ in F/g). Particularly, rGO showed C_{sp} ~ 200@1200cycles in electrolyte KOH [9-10], > 300@1000 cycles in PVA [11], ~ 600@ 1000 with electrolyte H_2SO_4 [12] respectively.

Similarly, MoS_2 layers alone shows ability to store electrostatic charge by electrode double layer capacitance (ELDC) mechanism. However suffers from inferior electrochemical performance in terms of poor cyclic life, inherently low charge transport, large volume change during cycling, and restacking.[13-14] yielding C_{sp} ~100 F g^{-1} @ 1 mV s^{-1} (scan rate).[15] In order to overcome this issues it has been mixed, wrapped or deposited with highly conductive/electro active materials such as carbonaceous materials or conducting polymers using various top-down/bottom-up synthetic as well as combinatorial approaches.[16-25]

Pristine h-BN, being electrical insulator does not suitably fit in this branch of application. But due to structural similarity with graphene and comparatively weak van der walls forces offers strong ionic bond and expected to provide superior C_{sp} if combine with graphene and MoS_2. [26]

There are many reports for binary composites. Further, binary composites of rGO are reported to show excellent electrochemical properties. The work carried out by Jiao et al in which MoS_2/rGO composite prepared via hydrothermal delivered excellent electrochemical properties with almost 95% of capacitance retention. [27] In another work reported by Zho et al MoS_2/rGO showed superior electrochemical properties with specific capacitance more than 1200F/g. [28] The layer controlled MoS_2/graphene aerogel composite also reported to show reversible capacity with specific capacitance more than 1000 mA/g at current density of 100mA/g. [29]

The focus of our current work is to investigate the electrochemical parameters of rGO/h-BN/MoS_2 hetro structure. This self-assembled composite is prepared by facile addition of equal volume ratios. The blend showed successful formation of composite 2D material. The electrochemical properties studied to realize the effect of blend of all 2D materials having C_{sp} > 650 Fg^{-1}(current density) with highest E_D >90+ Wh kg^{-1} and P_D 1700 W kg^{-1}. The combination studied, herein, not been reported thus far for their electrochemical applications. The details are presented.

View Article Online
DOI: 10.1039/D0NA00021C

2. Experimental section:

2.1 Reagents: Natural graphite flakes purchased from sigma Aldrich. All other reagents are analytical grade chemicals.

2.2 Preparation of rGO/MoS_2/h-BN multi-layered material: GMH-composite

Initially, graphene oxide (GO) was prepared from the natural graphite precursor by modified hummer route [30] GO has been washed with DI water for the several times in order made obtained GO free from the acidic moieties. Hexagonal boron nitride (h-BN) was prepared according to the protocols given in [31]. For this, around 3 g of boric acid (HBO_3), and approximately 9 g of urea mixed in the acetone and stirred the solution for 15 m or so. Following this, acetone was allowed to evaporate under natural conditions and the obtained powder was heated for ~ 700°C for 5 h, under nitrogen atmosphere. In a round bottom flask, subsequently, GO (500 mg), h-BN (500 mg), ammonium molybdate ($(NH_4)_6Mo_7O_{24}$-$4H_2O$, (1.25 g) and Thiourea (CH_4-NH_2S, 2.31 g) was added into the DI water [32]. In the reaction mixture, hydrazine hydrate (10 ml) was added and entire system was kept for heating at ~ 80°C into an oil bath for about 4 h. After this, the system was allowed to cool down to room temperature. During synthesis of h-BN, the small amount of B_2O_3 formed may be reduced in presence of hydrazine hydrate. Moreover, we prepared MoS_2, in-situ, in the reduction process of GO. The water was separated using vacuum filtration and the *black coloured* residue was washed using hot DI water and ethanol, sequentially. The residue was sonicated, further, for about 4 h to exfoliate the interlayers. Finally, the product was assumed to be multi-layered rGO/MoS_2/h-BN and *termed as* GMH-composite material. It was further characterized for the structure-property relationship and for its electrochemical applications studies.

2.3 Characterizations on GMH-composite:

Electron spectroscopy for chemical analysis (ESCA) measurements were performed using an Omricron ESCA probe (Omricron nanotechnology). X-ray powder diffraction studies carried out using Rigaku instrument with Cu K_α radiation (1.5406

View Article Online
DOI: 10.1039/D0NA00021C

A°) over 2θ range 10-90° @ scanning rate 2° m^{-1}. FTIR measurements were performed at 400-4000 cm^{-1}, using Bruker Tensor 37 and Raman over 200-3500 cm^{-1} using LABRAM HR 800 (@ λ ~ 533 nm). Nanostructure imaging was carried out by field emission scanning (FSEM, S-4700), high resolution transmission electron microscopy (HRTEM, JEOL-2100F) and energy dispersive X-ray (EDAX) elemental mapping. ESR measurements were performed at 9.4 GHz (X–band) with microwave input 950μW.

2.4. Electrochemical measurements:

The electrochemical performance of GMH was carried out using cyclic voltammetry (CV), and galvanostatic charge-discharge (CD) studies. In order to understand various impedance factors experienced by the electrode/electrolyte interface and charge transfer process, electrochemical impedance spectroscopy (EIS, Ivium Technology, Vertex) @ 0.1–10^6 Hz measurements were performed. All studies were carried out using Auto Lab (PGSTAT 30, Eco Chemie), at room temperature. Electrode preparation was done as per the protocols given in [33] The composite of GMH and polyvinylidene Fluoride (PVDF) were mixed solvent N-Methyl -2- pyrorolidone (NMP) in a ratio of 9:1 and slurry was dropped onto the glassy carbon electrode using the drop cast technique. The electrode was dried to perform CV, CD and EIS measurements. In CV measurement the three electrodes used are platinum wire as a: counter, Ag/AgCl: reference, and CNS: working electrode. The CV curves were obtained in a potential window of 0.2 to 0.8 V @ scan rates of 10, 50, 100, 300,500 and 1000 mVs^{-1}. In similar fashion, two-electrode CV measurements were performed in addition to constant CD measurements @1.0 to 3.5 $A\text{-}g^{-1}$. The electrolytes used were H_2SO_4 (1M), Na_2SO_4 (1M), Co_2SO_4 (1M). The cyclic stability of the cell was investigated up-to 20000 cycles@1A/g.

3. Results and discussions

3.1 Structure-property relationship: pre-analysis of GMH-blends

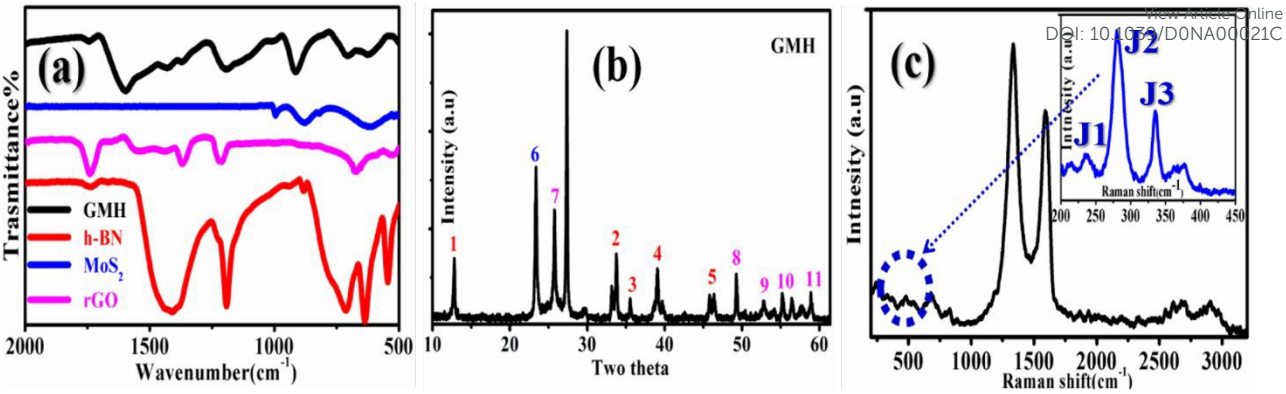

Figure 1: (a) FTIR spectra of individual components and composite of GMH, (b) XRD pattern of composite (numbers with colour show characteristic peaks of respective component), and (c) Raman spectra, recorded at 533 nm, for composite (zoomed portion of dotted circle connects typical J1, J2 and J3 peaks, the characteristic Raman features for 1T-MoS_2: inset).

Figure 1(a) shows recorded FTIR spectra of MoS_2, rGO, h-BN, and GMH-composites. For h-BN, a typically broad B-N peak appeared at ~ 1400 cm^{-1} displaying in-plane B-N-B stretching (str.), whereas, the peak ~ 750 shows out-of-plane B-N-B stretching. For rGO, peaks appeared at 1300-1500 are assigned to C-C str. and C-H bend, whereas, peak ~ 665 shows C-H out-of-plane vibrations. In MoS_2, peak at ~ 615 is due to presence of Mo-S str. In addition, profile shows small peaks at ~ 950, and 850 dues to Mo-O str. and shown as inset to corresponding zoomed region in plot(c). They are also shifted to lower wavelength supporting to composite formation. Their presence may be due to atmospheric handling of the material. However, IR profile of GMH-composite shows the features of individual components like peak at ~ 1600 due to C=C str. In composites, the peaks associated to B-N, C-C, and C-H seems to be over-lapped due to similar vibration frequencies, hence, bands appearing at 1300-1500 are attributed to their presence. A sharp peak at 900 is observed assigned to Mo-O, 700 to B-N-B, and ~ 630 to Mo-S stretching vibrations. Primarily the prepared composite shows the vibration features of individual MoS_2, MoO_3, h-BN, and reduced graphene oxide 2D layers. Further, the plot (b) is recorded XRD pattern of the composite obtained on calcination at 350°C that shows distinct diffraction peaks associated to rGO, h-BN and MoS_2 in the blend. The individual XRD patterns are provided in Supplementary information. For MoS_2, namely, peaks 1-5 matches with the JCPDS card no. 37-1492. The values for 2θ are ~ 12° (1), 33° (2), 33° (3), and 39° (4) , 42° (5)with corresponding Miller planes (0 0 2), (1 0 0), (1 0 3), (1 0 5) (1 1 0). The intensity for these

View Article Online
DOI: 10.1039/D0NA00021C

lines is observed to be low due to exfoliation and intercalation within layers of rGO and h-BN and indicative of lowering down of the number of layers. [34] Moreover, h-BN and rGO have very similar crystal structures with a very small lattice constant mismatch of ~ 2%. So, the main peaks have similar position as well as intensity. For rGO, they are indicated by number 6. The broad peak shifted to sharp crystalline at 2θ = 23.34° is indicative of rGO corresponding to d spacing of 0.326nm. During formation of heterostructure d spacing of rGO in blend is reduced almost to half. The lattice structure which is, significantly, different from the pristine graphite flake shows substantial exfoliation of conjugated 2D carbon layers. For h-BN the XRD pattern matches with JCPDs card number 73-2095 shown in figure 7-11. The corresponding planes matching are (1 0 0), (1 0 1), (0 0 4), (1 1 0) shown by numbers [35]. To summarize, composite of GMH shows presence of multi-layered heterostructure h-BN/MoS_2/rGO, as desired for electrochemical applications. Plot (c) shows Raman spectrum recorded at excitation wavelength 533 nm for the composite. Inset shows magnified region of 240-450 cm^{-1} in which 4 peaks are identified for MoS_2 have been, clearly, identified. The D band at 1340 cm^{-1} with intensity higher than G, appeared at, 1590 cm^{-1} indicates presence of impurity induced due to MoS_2 and h-BN. In addition, the 2D doublets have been registered in the blend at ~ 2700. The h-BN shows characteristic peak at 1370 which is due to E^2g phonon mode and similar to the mode associated with D band in graphene [36] In composite samples, their presence is not seen separately due to mutual overlap, however, resulted into a mixed band to somewhat lower wavelength at 1340. The position of D band is also shifted to lower wavelength [37]. MoS_2 has characteristic band appeared at 280 ,335, 370, 418 cm^{-1}. The bands at 370, 418 cm^{-1} which are attributed, respectively, to E^1_{2g} and A^1_g modes while major characteristic peaks at 280 ,335 cm^{-1} belong to E_{1g} and Longitudinal acoustic phonon mode respectively. These three peaks are bestowed with the 1T phase of MoS_2. It indicates that during composite formation 1T phase is formed may be for the better structural stability of MoS_2. [38,39]

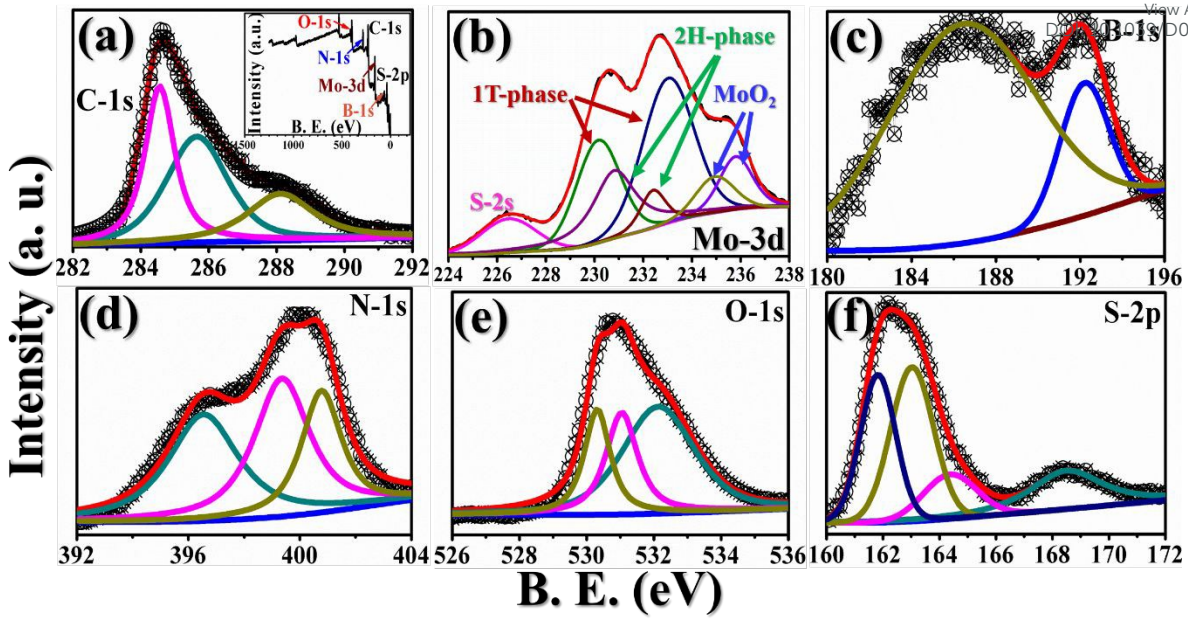

Figure 2: Recorded XPS spectra for GMH-composite in which (a) C-1s (Inset: elemental survey scan), (b) Mo-3d (indicating 1T, 2H and oxide states), (c) B-1s, (d) N-1s, (e) O-1s, and (f) S-2p.

In order to understand the surface chemical composition and the valence state of the GMH blend, XPS analysis has been carried out. Figure 2 shows corresponding spectra. Inset of plot (a) shows survey spectrum indicating coexistence of the elements such as B, S, Mo, C, N, and O in GMH. Further, composition of MoS_2, in GMH, was confirmed by the high resolution of MoS_2 spectrum shown in plot (b). For Mo-3d envelop, one can have deconvolutions upto four peak fits at binding energies 226.5, 230.4, 232.8, and 235.2eV. The peak at 230.4 is assigned to Mo (+4) 3d 5/2 and 232.8 for 3d 3/2 with spin-orbit coupling separation nearly 2.4eV. The shift of these additional peaks suggests that they arise from the 1T phase. This can be identified to be metallic 1T phase partially mixed with oxidized MoS_2 which is consistent with Raman analysis. [39]. The peak at 235.05 is assigned to respective Mo (+6) 3d electronic shell. The emergence of such peak may be due to the exposure of MoS_2 to air showing presence of MoO_3 or may be incomplete reduction of Mo(+6)(R-2016, 6, 74436). In addition, peak at binding energy of 226.4eV, corresponds S 2s of MoS_2 and is also shows its resemblance in spectral region of S-2p (plot (f)). For sulphur, peaks at 161.8 and 163.04 are assigned to Mo-S bonding with spin-orbit coupling ~ 1.24eV. Moreover, in (f), the spectrum shows that the binding energy of S-2p 3/2 is 161.9 which correspond to charge state of S as −2 in MoS_2. Further, the peak at 164.3 corresponds to C-S bonding, whereas, the peak

View Article Online
DOI: 10.1039/D0NA00021C

at 168.5 corresponds to carbon-sulfonate bonding. While in plot (e), O-1s is deconvoluted for three components at 532.2, 531.04, and 530.3eV that, broadly, corresponds to C-O and M-O bonding. In plot (a), C-1s envelop is fitted for three peaks. Particularly, peak at 284.5eV which appears to be broad having asymmetric tail towards the higher binding energy side shows high concentration of sp^2 contents in rGO. While other peaks at 285.6, and 288.15eV at a difference of 1-2 eV shows presence of sp^3 fraction emerging from C-O, and C=O components, respectively. In plot (d), N-1s spectrum is fitted for three components in which the main broad peak at 396.5 is attributed to N-B bonding in h-BN, whereas, the other centred at ~ 400 has been identified as the presence of N-H bond or amide group [40], and peak at ~ 401 shows C-N bond. In plot (c), the deconvoluted B-1s spectrum indicates the existence of sp^2-like phase in B–N due to peaks appeared at ~ 193 and ~ 187 eV. They show substitution of boron sites that exist in the rGO network of GMH composite. [41,42].

In analysis of GMH composite, broadly, excess of oxygen containing groups are significantly reduced and only small amount of oxygen is observed to be resided into the 2D multilayers. From rGO, h-BN and MoS_2 sheets the unwanted traces of, respectively, hydroxide /epoxide, B_2O_3, MoO_3 are removed due to action of hydrazine hydrate as a reducing agent. The blend is found to be rich in C-B-C, Mo-S, C-N, B-N, Mo-C, etc., molecular bonding forming composite formation of composite layers.

3.2 Morphological analysis of GMH blend

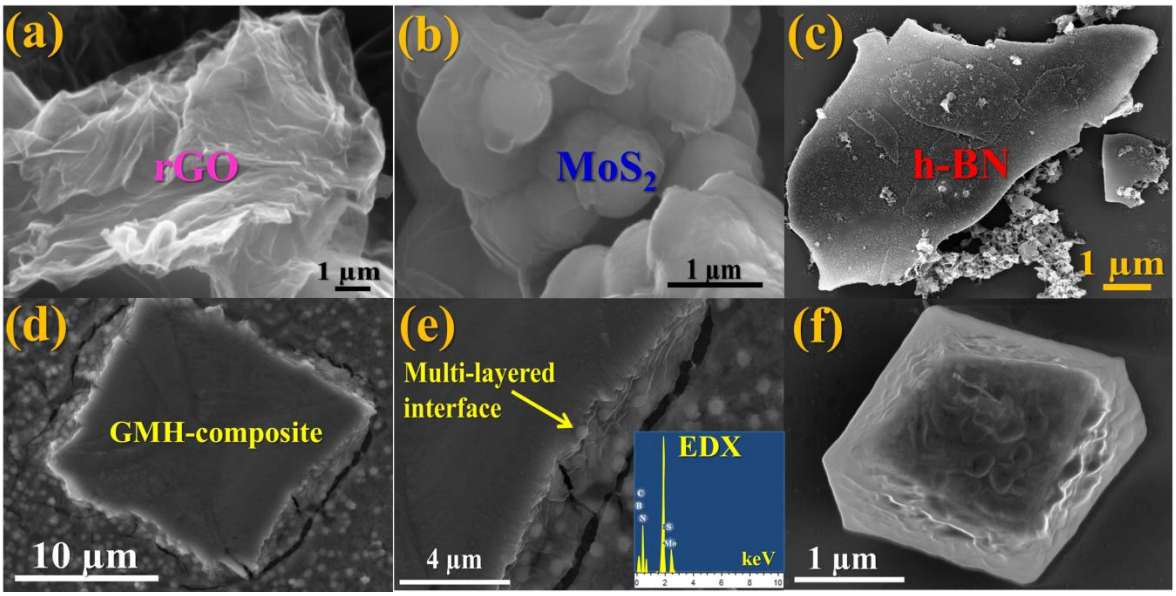

View Article Online
DOI: 10.1039/D0NA00021C

Figure 3: Typical FESEM images. Upper panel shows individual 2D layers of (a) rGO, MoS_2, and (c) h-BN. Lower pan: (d) GMH-composites, (e) sandwiched layers and inset EDAX revealing elemental composition, (f) smaller block of blend.

The electron microscopy imaging analysis has been carried out in order to investigate morphology of GMH-composite. Figure 3 shows typical FESEM images of rGO, MoS_2, h-BN and GMH and EDX spectrum of GMH. FESEM image of rGO. Figure 3(a) shows smooth, homogeneous surface with typical wrinkles of rGO sheets that cause sheet folding. The corrugation and scrolling represent the intrinsic nature of graphene, because the 2D membrane structure would be thermodynamically stable via blending with the corrugation and scrolling. [34 36] Figure 3(b) shows coalesced plate-like MoS_2 particles. It is seen that these microspheres are stacked by nanosheets assembled of uniform nanospheres. These nano spheres like sheet inter cross loose and having void space between them. Part(c) shows FESEM image of h-BN indicating sharp edges, flat surface and smooth surface. However, in case of FESEM images of GMH show entirely different morphology. It is shown in part (d) layered structure likes lumps can be seen. It is observed that compact packing and layers of rGO are seems to be broken down into small layers. For GMH micrograph of cross section part (e) and part (f) it is seen that 2D planes are tightly stacked and the layered structure is well preserved with h-BN and MoS_2 planes sandwiched in between the layers. The tightly packed layered structure plays a key role in the efficient charge transfer as well as storing of between three nanosheets.

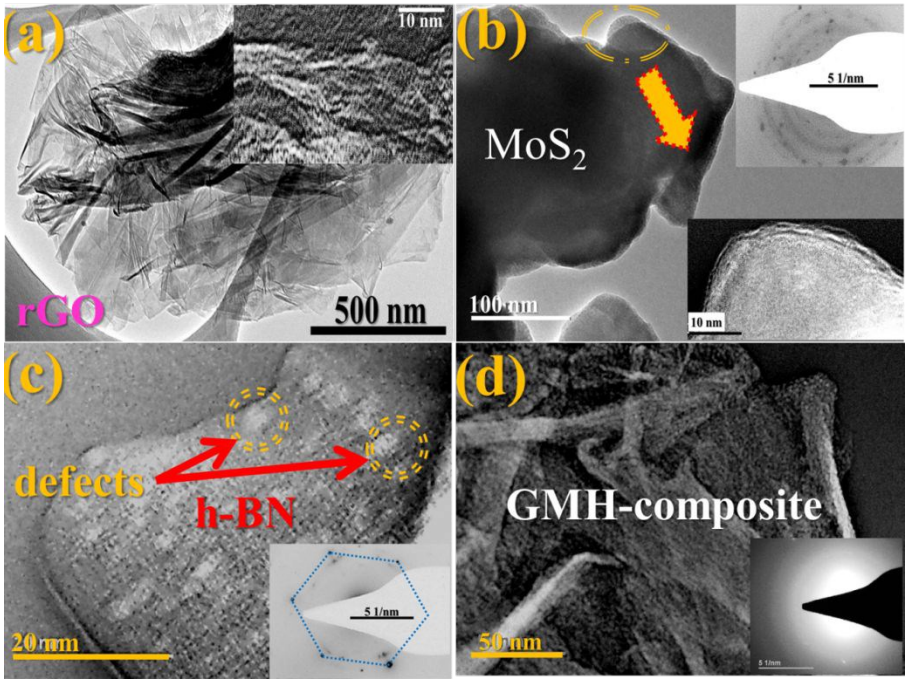

View Article Online
DOI: 10.1039/D0NA00021C

Figure 4: Typical HRTEM images for (a) rGO (inset: higher resolution of layers), (b) MoS_2 (inset: higher resolution and SAED pattern), (c) h-BN arrows and double circles show defects (inset corresponding SAED), and (d) GMH-composite with SAED.

Figure 4 (a) Image shows a typical TEM image of rGO, indicating well-defined graphitic planes stacked and respective inset displays higher resolution imaging with lattice fringes. It indicates notable crystallization of the sheets. Image (b) shows two layers of MoS_2 and it seems that due to stacking fault the crystallinity is somewhat lost. In (c), crystalline h-BN is seen with some structural defects shown by yellow double circles. The defects could be attributed to presence of B_2O_3. They could be passivated as we add more amount of hydrazine hydrate as discussed previously. Corresponding, inset shows SAED pattern which confirms crystallinity of h-BN. Image (d) shows stacked compact layers of rGO, MoS_2 and h-BN and SAED pattern shows amorphous nature of blend. The supercapacitor performance of GMH-composite was investigated by Cyclic Voltammetry (CV) studies.

3.4 Electrochemical studies

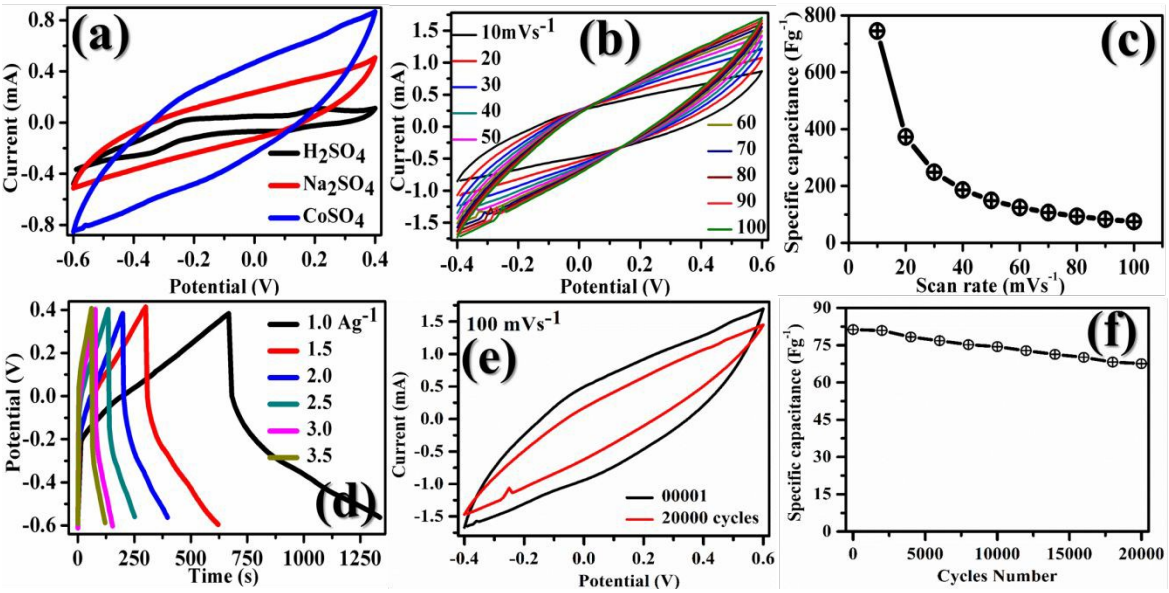

Figure 5: CV measurements on GMH-composite for (a) different aqueous electrolytes (scan rate@ 10 mVs^{-1}) with superior performance in $CoSO_4$, (b) variable scan rates between 10-100 mVs^{-1}, (c) change in C_{SP} (specific capacitance) with scan rate, (d) stability curve upto 20000 cycles, (e) CV curves recorded after the first and the last cycle, (f) charge-discharge (CD) curves at variable current density (Ag^{-1}). Plot (b)-(f) are CV measurements in $CoSO_4$ electrolyte.

View Article Online
DOI: 10.1039/D0NA00021C

Figure 5, plot (a) shows three electrode CV curves obtained for GMH-composites in different aqueous electrolyte at scan rate of 10 mVs^{-1}. The values of the specific capacitance, C_{SP}, measured in Fg^{-1}, were recorded to be 302.67, 564.18, and 745.18 for electrolytes H_2SO_4, Na_2SO_4, and $CoSO_4$, respectively. They were calculated using the relation: $C_{sp} = \frac{\int iv.dV}{2\mu m \times \Delta V}$. The magnitude for C_{sp} in H_2SO_4, electrolyte is low and shape of CV curve somewhat distorted. It may be due to corrosive nature of acid towards metallic species present in composite. The use of acidic or basic medium electrolytes can be act as current collectors, connexions. In order to overcome such technical drawbacks, they should be avoided [39]. With neutral electrolyte such as Na_2SO_4, and $CoSO_4$ showed symmetric current potential characters meaning ideal capacitive behaviour. In general, the process of oxidation and reduction during cycling depends on physical parameters of cations such as charge, charge density and size. [40]. The highest value C_{sp} is obtained for $CoSO_4$ and used for further analysis. This is attributed low cationic radii of Co^{2+} ion (0.72 Å) than that of Na^+ (0.99Å). Plot (b), represents profiles (three electrodes) at various scan rates 10-100 mVs^{-1} in $CoSO_4$ electrolyte. The CV curves exhibited nearly rectangular shape and indicative of an ideal electrode double layer capacitor. From the device perspective it is important to investigate two electrode CV measurements. So, we have proceeded for this, in (c), variations in C_{SP} with change in scan rate has been observed to study the effective interaction between the ions and the electrode. Further, plot (IV) shows galvanostatic charge discharge curves at various current densities 1 to 3.5 A g^{-1}. The increase scan rate as well as current density shows decrease in specific capacitance.

Table 1 shows specific capacitance, C_{SP}, for two electrodes technique with corresponding power, P_D and energy density, E_D. The values of C_{SP} in two electrodes are usually less as compared to three electrodes configuration and calculated using the formulae:

$$C_{sp} = 4 \times \frac{I\Delta t}{m\Delta V} \quad (1)$$

$$E_D = \frac{1}{2} \times \frac{1}{4} \times \frac{1}{1.36} \times C_{sp} \times \Delta V^2 \quad (2)$$

$$P_D = \frac{E}{\Delta t} \quad (3)$$

Where, I, is current, m, is specific mass, Δt, is time, and ΔV, potential window.

Table 1: Calculated C_{SP}, E_D and P_D for GMH composite for two electrodes system.

Current density (Ag^{-1})	1.0	1.5	2.0	2.5	3.0	3.5

View Article Online
DOI: 10.1039/D0NA00021C

C_{SP} (Fg^{-1})	683	482	401	296	224	214
E_D ($Whkg^{-1}$)	92.3	65.1	54.2	40.0	30.0	28.9
P_D (Wkg^{-1})	486	729	972	1213	1458	1701

At lower current density (lower scan rate), both the inner/outer active sites and pores of GMH would be sufficiently accessed by the electrolytic ions and leading to high C_{SP} value. For high current density or scan rate only external surface of electrode material contributes to charge/discharge process. It seems that, nano sheets during CD process significantly shorten down the ion diffusion pathways and helped in obtaining the high specific capacitance [36]. Figure 5 (e) and (f), respectively, shows I-V curves, after 1 and 20,000 cycles. After 20,000 cycles a slight decrease in specific capacitance is observed by ~ 25% or so with reduction in area under the curve. The good cyclic stability can be attributed to their excellent chemical stability, mechanical strength and flexibility of GMH composite. [43]

Table 2 provides comparison of the other class of supercapacitors performance reported previously over the current work. Typically, carbonaceous materials like graphene, carbon nanotubes, carbon aerogel, etc. have high electrical conductivity and surface area. Developing TMD hybrids or composite materials with carbon-based materials provides a synergistic effect of the two materials; carbon offers conductive channels and enhancing interfacial contact, while TMDs contribute a short ion diffusion path and successive short electron transport path. In comparison it shows good retention stability of 75% up to 20,000 cycles.

After cycling, GMH composite is analysed with XPS and it has been observed that the chemical environment of heterostructures is same as that of pristine samples as seen in Fig 6.

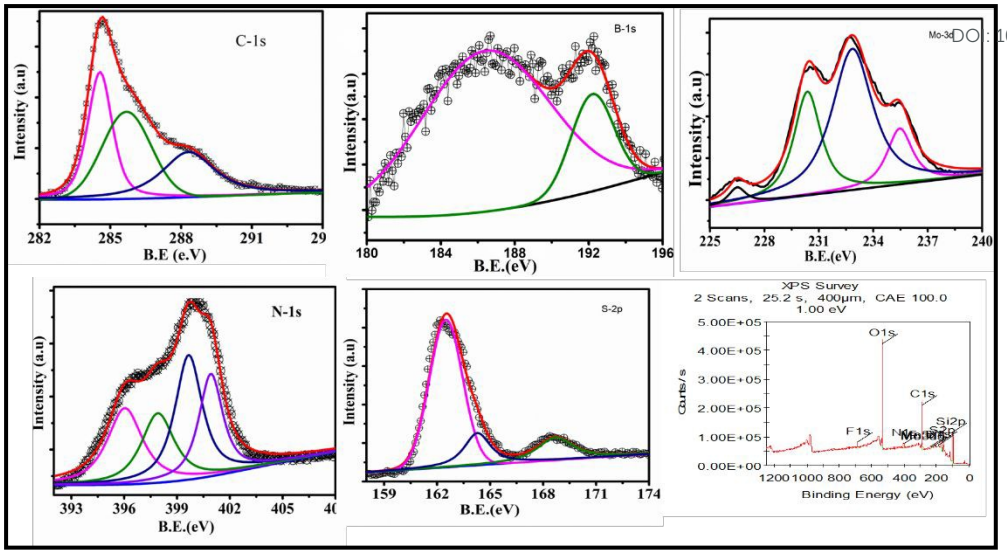

Figure 6: Recorded XPS spectra for GMH-heterostructure after 20,000 cycles.

It seems that, inter-layer electrostatic *cross-talk* might be playing important role when one shade light on the mechanism of charging-discharging of such multi-layered blend made up of rGO, MoS_2 and h-BN. The inter-layer stacking of MoS_2, h-BN in conjugation with rGO layers may be mutually acting as the spacer molecular layers that prevent restacking. Further free radical electrons may be responsible for changing oxidation state of intercalated Mo, B, N and S atoms which contributes to the additional charge storage capacity of the blend. On the other hand, intercalated MoS_2 provides additional channels for charge transport and increases the overall conductivity of the electrodes.

Table 2: Performance characteristics of reported supercapacitors over current work

Electrode material	Electrolyte	C_{SP} (Fg^{-1})	Cyclic stability	E_D ($Wh\ Kg^{-1}$)	P_D (KWg^{-1})	Ref.
MoS_2-rGO	1M Na_2SO_4	388@1.2Ag^{-1}	100 % upto 1000 cycles			[44]
h-BN/rGO	6M KOH	145@6Ag^{-1}	89% upto 40000 cycles	40	4200	[26]
Graphene/ MnO_2	Ethanol	315	95% upto 5000 cycles	13	110	[45]
Aloe-vera derived carbon	[EMIM][BF_4]	244	83% upto 500 cycles	40	-	[46]

MoS_2/rGO	2M KOH	220@ 1Ag^{-1}	91.8% upto 1000 cycles	-	-	[47]
Te/rGO	1M H_2SO_4	260F/g @0.25A/g)	~80% up to 10000	8	250	[48]
GMH-composite	$CoSO_4$	215@3.5Ag^{-1}	75%upto 20,000 cycles	30	1700	Current work

The re-hybridization of MoS_2 may also be possible with h-BN. This may allow the intercalated ions to move swiftly providing the active charging sites. The dominant electrical double layer capacitor (EDLC) behaviour of the composite GMH electrodes is synergistic effect of kinetics for non-faradaic proton adsorption at the interface of MoS_2/h-BN/rGO. Figure7 shows (a) Nyquist and corresponding (b) Bode plot recorded for GMH blend. The impedance analysis is employed to study the frequency of characteristic of electrode. The EIS was carried out in 2M $CoSO_4$ solution over the frequency range of 0.01-10,000 Hz.

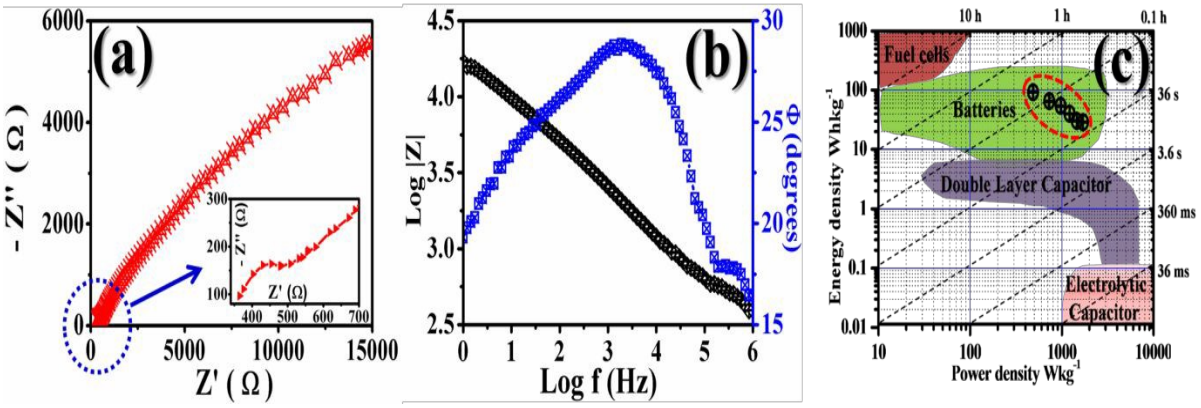

Figure 7: (a) Nyquist (arrow shows inset), (b) Bode and (c) Ragone plot (dotted circle our results) for GMH electrodes.

The impedance spectrum of GMH in high frequency region exhibits a semicircle with low diameter and straight line in low frequency region. The intersection of real axis in high frequency region represents the solution resistance R_s and related charge transfer frequency between the electrode material and electrolyte. The value of R_s is found to be very low ~ 5Ω indicating the nature of electrode is highly conducting. The low solution resistance suggests that GMH cell can be assembled in a series for high voltage application with minimum loss of energy. Further, presence of straight line in high frequency region shows ideal

View Article Online
DOI: 10.1039/D0NA00021C

supercapacitor behaviour**.** Inset shows enlarged plot at almost board curved line instead of semicircle which is due to very low faradic resistance indicative of pseudo capacitive**.**

In order to understand frequency dependant impedance characteristic of GMH electrode the logarithm of absolute impedance, |Z| and phase shift Φ is studied. Almost linear nature is indicative of swift electron exchange at the solution/electrolyte interface. The two phase angles at 30° and 5° is found mid and low frequency region showing pseudo capacitive behaviour of the blend electrode. It may be due to diffusive characteristic of electrode electrons.

Ragone plots are used to compare the performances of the current surfaces, showing the relation between power density, P_D and energy density, E_D. The calculated power density is 486, 729, 1213, 1458, 1701 W Kg^{-1} and energy density $Whkg^{-1}$ 92.3, 65.1, 54.2, 30, 28.9 respectively with various current density @ 1, 1.5, 2, 2.5,3, 3.5 Ag^{-1}. The values of C_s, P_D, E_D shown in table compared with reported forms of carbon. The material shows good performance in the aqueous solution where the pore accessibility becomes a limit on energy excitation at higher powers. The Ragone plot shows utility of GMH at battery in the region of battery application. So as prepared composite material, GMH finds suitable application as ideal electrode material for batteries. The parametric values obtained from the fitting are shown in Table 3.

In Nyquist study, the semicircle pattern is obtained with supressed shape (shown in respective inset) above real axis. Using the data values of real and imaginary |Z|, circuit model is simulated and best fitted for their discrete components like impedance (R), inductance (L), charge accumulated (Q). The simulated circuit is superimposed on to GMH heterostructure and schematically shown in Fig 8. The impedance component, being complex entity could be represented in terms of constant phase element due to the semi-circular pattern obtained in Nquist plot.

View Article Online
DOI: 10.1039/D0NA00021C

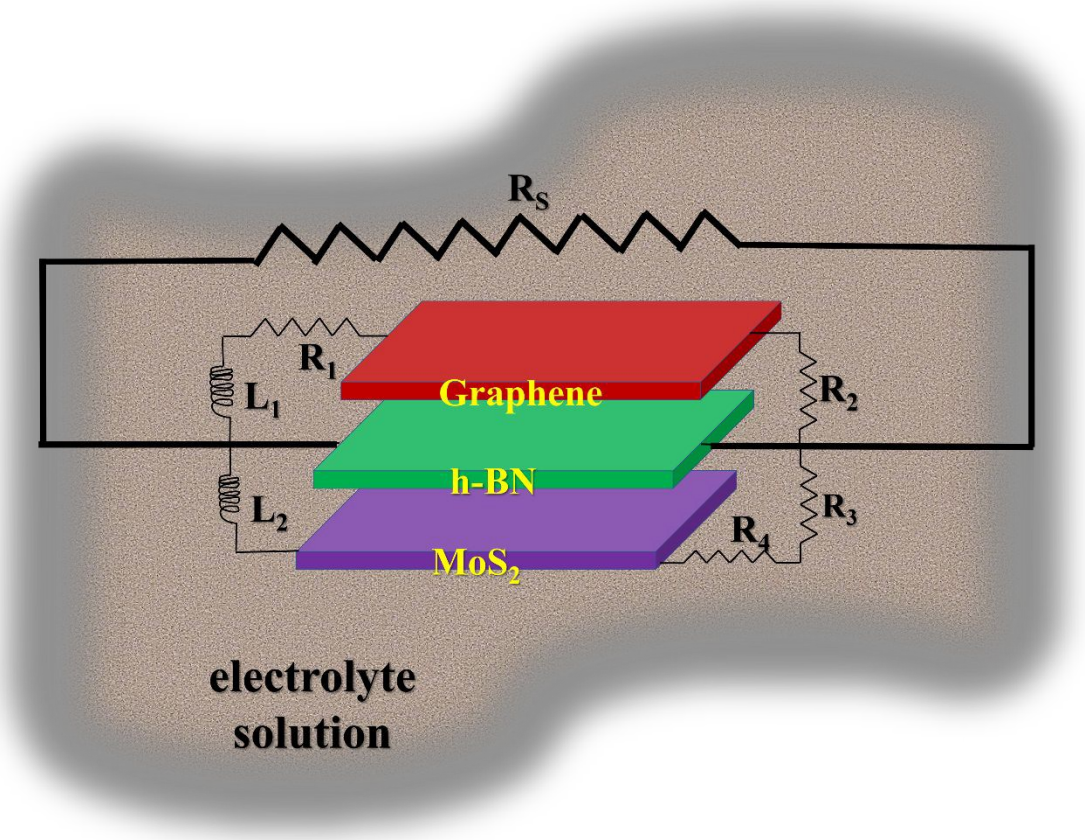

Figure 8: Schematics of GMH-blend electrode in electrolyte superimposed on simulated equivalent circuit.

From the schematic one can see that, equivalent circuit is composed of series of impedance arising because of GMH interface, their respective surfaces, capacitive components (neglected during simulation), their interfacing with solution resistance, mutual inductance arising from highly conducting graphene / MoS_2, effective charge accumulating grain boundary. Notably the sequence of self-assembled heterostructure is immaterial. All this together with constant phasor element lead to the equation:

$$Z_{eff} = Z^{-\alpha} \times L^{\beta} \times Q_{GMH}^{-1}$$

Where, Symbol have their usual meaning and indices shows series/parallel components.

the parameters obtained for discrete components by circuit simulation is shown in Table 3. one can see that impedance, $Z^{-\alpha}$, systematically increases form bulk solution to

self-assembled heterostructure electrodes including charge accumulation dynamics, Q_{GMH}. Both muctual inductances, L^{β}, increased further by the factor of two in the case of the rGO/h-BN and h-BN/MoS_2, indicating strong synergistic effects because of the combination of the two materials, that is, MoS_2 and h-BN.

Table 3. Circuit parameters generated after the fitting to a simulated equivalent circuit

Parameters	Magnitude with units	Error (%)	Parameters	Magnitude with units	Error (%)
Z_s	0.30 kΩ	10.00	Q_S	0.10 milli stat C	07.00
Z_1	0.50 kΩ	10.50	$Q_{S\text{-}GMH}$	0.32 stat C	04.50
Z_2	1.50 kΩ	13.00	Q_G	0.01 stat C	01.75
Z_3	2.50 kΩ	23.00	Q_{eff}	03.18 milli stat C	16.00
Z_4	3.00 kΩ	06.70	L_1	14.61 mH	03.82
Z_5	3.50 kΩ	10.00	L_2	28.74 mH	04.50

Further, electron spin resonance spectroscopy (ESR) reveals dynamics of radical electron in a solid system resonating para-magnetically by absorption of microwave energy. The purpose of ESR analysis is to estimate diffusion dynamics of such radical electrons in GMH blend vis-a-vis their individual counterparts.

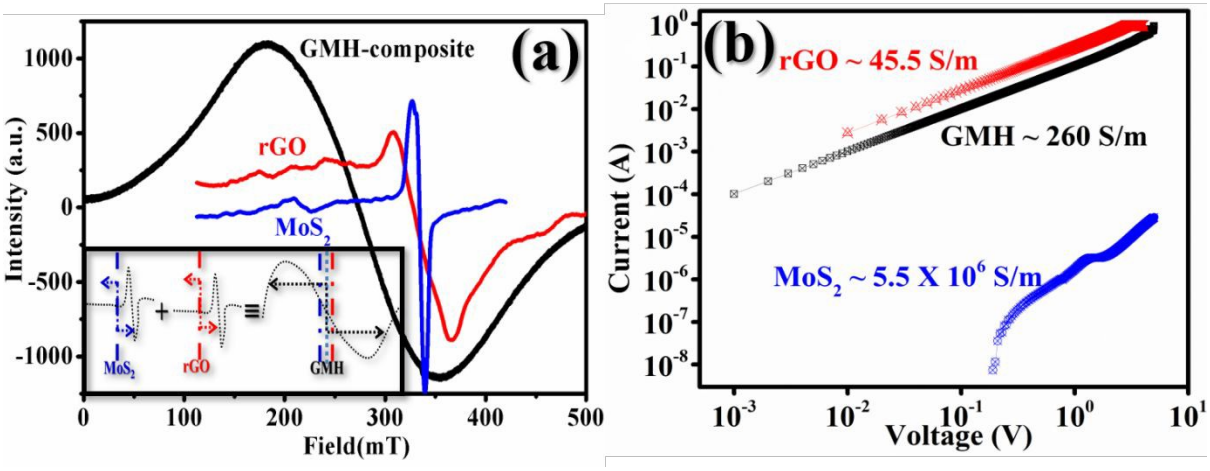

Figure 9: (a) Recorded electron spin resonance profiles for rGO, MoS_2, GMH–composite@ 300K. Inset shows scheme for electron diffusion for the individual 2D materials and its

View Article Online
DOI: 10.1039/D0NA00021C

composite. Arrows indicate, schematically, electron diffusion length, D_L, during charging in MOS_2, rGO, and GMH-composite, respectively, 200, 600, and 1500 μm. (b) recorded I-V profiles for rGO, MoS_2, GMH–composite@ 300K indicating specific conductance. In both measurements profiles for h-BN is not obtained.

As a first step towards computing electron transport parameters is magnitude of the line width is determined by peak to peak distance, ΔH_{pp}, and shape of the ESR spectra are investigated. Figure 9 shows variation in intensity with applied magnetic field for rGO, MoS_2 and GMH-composite at room temperature. ESR spectrum of h-BN is not obtained. In case of rGO, MoS_2 the first absorption derivative dY/ dH as a function of applied field shows unsymmetrical nature while for GMH composite symmetric and homogenous peaks are observed. Further the principal parameter governing spintronics usability is the spin-lattice relaxation time T_{sl} which characterize non thermal spin states around the lattice. From the measured values of ΔH_{pp}, and using: $1/T_{sl}$ = (28.0 GHz)/T (in K)) × ΔH_{pp}, the measures of T_{sl} and electron diffusion length, D_L, has been carried out with the assumption: Fermi velocity ~ 10^6 ms^{-1} in all 2D materials [47-50]. For MoS_2, the D_L is estimated to be ~ 200 μm, whereas, for rGO ~ 600 μm. the effective D_L is found to be ~ 1500 μm for GMH-composites. This indicates that, on charging electron diffusion is quite high for GMH compared with their individual components. Further this also supports the conductivity measurements.

Plot (b) shows the IV plots for rGO, MoS_2 and GMH using two probe conductivity measurements at room temperature. In case of h-BN as such no curve obtained. The calculated values for specific conductivity of prepared pallets of rGO, MoS_2 and GMH are 45.5±3.5, 5.5±15×10^6, and 260±30 S/m respectively. Specific conductivity of rGO is very high as compared to GMH and MoS_2. The observed decrease is due to presence of h-BN in the composite. Due to which the magnitude of T_{sl} and implications of D_L proves the composite material good for energy storage. Therefore, further we have prepared cell for GMH blend and performance is tested.

3.5 GMH-cell: performance

GMH blend has been implemented for active electrode material for laboratory scale demonstration of the *blend-cell* action. The electrodes are developed as described in [35]; Figure 10 (a) shows corresponding apparatus, starting materials, flat electrodes, etc. The

View Article Online
DOI: 10.1039/D0NA00021C

assembly is packed with an aluminium foil as seen in image (b). Prior to charging the voltage between two electrodes was measured and found to be negligibly small ~ 0.01mV or so. The assembly is connected to *crock-clips* having conducting wires. The cell is charged for about 1.5 min with nominal 12.50 V automobile battery. The voltage measured, instantaneously, is found to be ~ 12.30 V, after charging, as seen in image (c). The voltage fallen down gradually with time indicating recombination of developed charges across 2D materials. The Helmoz layer degradation time is found to be very small for such primitive assembly. The charging measurements are performed, repetitively. In one case we connected the assembly to a commercially available LED equipped with current carrying wires. The LED is found to be illuminated, seen in image (c) for a period of 5 min or so. The result shows laboratory scale performance of fabricated electrode using GMH molecular blend. No such effect is observed for rGO specimen prepared and tested in identical fashion.

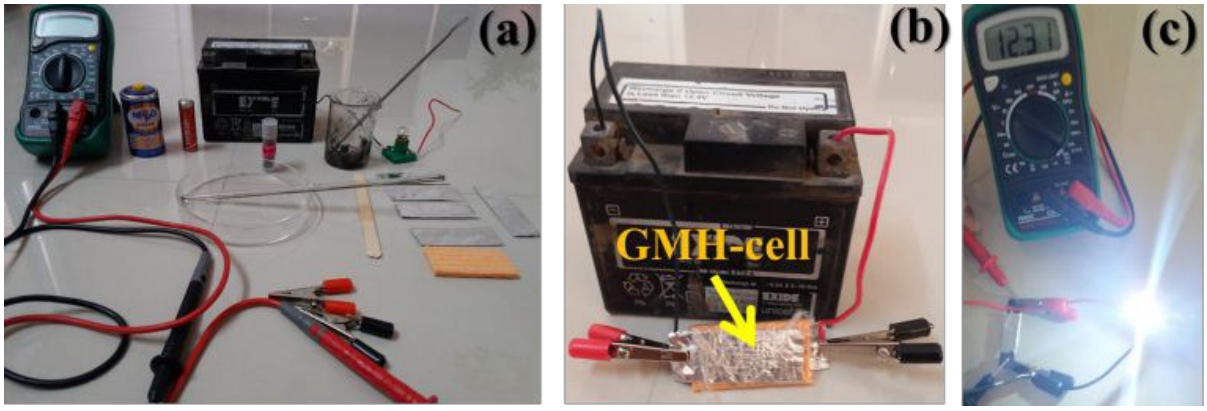

Figure 10: Laboratory scale demonstration of GMH electrode demonstrating LED illumination. (a) apparatus like substrate, digital multimeter, 12.4 V commercial automobile battery, active electrode material, carbon powder, PVDF, etc., (b) charging of the *blend-cell* with battery, (c) LED illumination after charging indicating voltage attained by the fully sealed fabricated blend electrode assembly.

Further ESCA analysis of GMH composite after 20,000 cycles revealed that there is no change in elemental composition of GMH. Supplementary information figure S1.

View Article Online
DOI: 10.1039/D0NA00021C

4. Conclusions

We have developed porous self-assembled nano-composite medium of 2D materials comprised of GMH, rGO, MoS_2, h-BN to use them as an active material for evaluating supercapacitor performance. The symmetrical EDLC electrodes were prepared using GMH blend showing highest $C_{sp} \sim 683$ F g^{-1} @ 1 Ag^{-1} (current density) with highest energy density, E_D, ~ 90 Wh kg^{-1} while power density, $P_D \sim 1700$ W Kg^{-1}. The ESR studies underlines that diffusion length of electron is increased to large extent which has effectively benefited the migration of electrolytic ions into multi-layered structures. The presence of small semicircle in high frequency region shows favourable solution resistance and effective charge transfer mechanism between blend to electrolyte. At high frequency the electrode shows tendency of ideal super capacitor compounded with marginally low faradic resistance. The phase angle at 30° and 5° in mid and low frequency region is indicative of hybrid behaviour as analysed by Bode. The Ragone analysis indicated electrode performance in region of battery like region. The present study suggests unique combination of GMH as an ideal material for high performance supercapacitor application.

View Article Online
DOI: 10.1039/D0NA00021C

References:

1 K. S. Kumar, N. Choudhary, Y. Jung, J. Thomas, *ACS Energy Letters*, 2018 ***3***, 482.

2 Z. Yu, L. Tetard, L. Zhai, J. Thomas, Energy & Environmental Science. 2015, 8,702

3 N. Choudhary, C. Li, J. Moore, N. Nagaiah, L. Zhai, Y. Jung, J. Thomas J. *Advanced Materials.* 2017 ,**21**, 1605336

4 M. Chhowalla, Z. Liu, H. Zhang, 2015. *Chem. Soc. Rev*. **44**, 2584.

5 Y. Hou, J. Li, Z. Wen, S. Cui, Yuan, J. Chen, 2014, *Nano Energy,* **8**, 157.

6 Y. Zhang, Y. Zheng, K. Rui, H. Hng, K.Hippalgaonkar, J. Xu, W. Sun, J. Zhu, Q.Yan, W.Huang, 2017,*Small*, **13**, 1700661

7 S. Zhang, F.Yao, L.Yang, F. Zhang, S.Xu, 2015, *Carbon* ,**93**, 143.

8 A. Lipatov, M. Alhabeb, M.R. Lukatskaya, A. Boson, Y. Gogotsi, A. Sinitskii, 2016, Adv. Electron. Mater., **2**, 1600255

9. Y. Wang, Z. Shi, Y. Huang, Y. Ma, C. Wang, M.Chen, Y. Chen .*The Journal of Physical Chemistry C*, 2009 ,**113**,13103.

10 V.L. Pushparaj, M.M. Shaijumon, A. Kumar, S. Murugesan, L.Ci, R. Vajtai, R.J. Linhardt, O. Nalamasu, P.M. Ajayan, 2007, **104**,13574.

11 C. Meng, C. Liu, L. Chen, C. Hu, S. Fan, *Nano letters*, 2010 ,10, 4025.

12 Z.S. Wu, D.W. Wang, W. Ren, J. Zhao, G. Zhou, F. Li, H.M. Cheng, *Advanced Functional Materials,* 2010 ,**20**, 3595.

13 F. Zhang, Y. Tang, H. Liu, H. Ji, J. Jiang, X. Zhang, C.S. Lee , *ACS Appl. Mater. Interfaces,* 2016 ,**8**,4691.

14 Y.Ge , R. Jalili, C. Wang ,T. Zheng, Y. Chao, G. G. Wallace, *Electrochim Acta*, 2017 235,348.

15 J.M. Soon, K.P. Loh, *Solid-State Lett*. 2007, **10**, A250.

16 M. Yang, J.M. Jeong, Y.S. Huh, B.G. Choi, *Compos Sci Technol*. 2015,**121**,123.

17 C. Yang, Z. Chen, I. Shakir, Y. Xu, H. Lu, *Nano Res*. 2016, **9**, 951.

18 M.A. Bissett, I.A. Kinloch, R.A. Dryfe, *ACS Appl. Mater. Interfaces*, 2015 **7**,17388.

19 S. Patil, A. Harle, S. Sathaye, K.Patil, *Cryst Eng Comm*. 2014, **6**,10845.

20 K. J Huang, L. Wang, Y.J. Liu, Y.M. Liu, H. B. Wang, T. Gan, L.L. Wang, Int. *J. Hydrog. Energy* 2013 ,**38,**14027.

21 J. Wang, Z.Wu, K.Hu, X. Chen, H.Yin, *J. Alloys Compd,* 2015, **619**,38.

22 G. Ma, H. Peng, J. Mu, H. Huang, X. Zhou, Z. Lei, 2013 ,**229**,72.

23 J. Wang, Z. Wu, H. Yin, W. Li, Y.Jiang , *RSC Advances*. 2014,**4**,56926.

24 T. W. Lin, T. Sadhasivam, A. Y. Wang, T. Y. Chen, J. Y. Lin, L. D. Shao, L. D. *ChemElectroChem*. 2018,***5***,1024.

25 T. W. Lin, M. C. Hsiao, A. Y. Wang, J. Y. Lin, *ChemElectroChem*. 2017,**4**, 620.

26 S. Saha, M.Jana, P. Khanra, P. Samanta, H. Koo, N.C Murmu, T. Kuila *ACS Appl. Mater. Interfaces*, 2015, **7**,14211.

27 N. Tronganh, Y. Yang, F. Chen, M. Lu, Y. Jiang, Y.Gao, L.Cheng, Ziao, *RSC advances*, 2016 *6*, 74436

28 L. Chen, Y. Yang, Y. Gao, N. Tronganh, F. Chen, M. Lu, Y.Jiang, Z.Jiao, B. Zhao., *RSC advances* 2016. ***6,*** 99833.

29 B. Zhao, Z.Wang, Y.Gao, L.Chen, M.Lu, Z. Jiao, Y.Jiang, Y.Ding, L.Cheng, *Applied Surface Science*, 2016, ***390,***209-215.

30 J.S. Hummers, William, R.E. Offeman, *J. Am. Chem. Soc* ,1958,**80**,1339.

31 L. M. Ansaloni, E.M.de Sousa, Mat*. Sci and Appl*. 2013,**4,** 22.

32 P.K. Panigrahi, A. Pathak *J of Nanoparticles*, 2013.

33 S.A. Haladkar, M.A. Desai, S.D. Sartale, P.S. Alegaonkar, *J. Mater. Chem. A*., 2018,**6**, 7246.

34 E.M.E Mora, 2017. New Icosahedral Boron Carbide Semiconductors (Doctoral dissertation, The University of Nebraska-Lincoln).

35 Y. Kang, Z. Chu, D. Zhang, G. Li, Z. Jiang, H. Cheng, X. Li, 2013, *Carbon,* **61**,200.

36 Z. L. Wang, D. Xu, Y. Huang, Z. Wu, L.M Wang, X.B. Zhang, 2012, *Chem Comm*, 48, 976.

37 M.P. Bichat, E. Raymundo-Piñero, F. Béguin, 2010, *Carbon*, **48**, 4351.

38 Y. Yao , K. Ao, P. Lv , Q.Wei, 2019, *Nanomaterials,* **9**, 844.

39 G. Eda, H.Yamaguchi, D. Voiry, T.Fujita, M. Chen, M. Chhowalla, 2011, *Nano Lett*. **11**, 5111.

40 Y.M.Cai, Z.Y. Qin, C. ong, 2011, *Pro Nat Sci-Mater*, **21**,460-466.

41V.H. Pham, K.H. Kim, D.W. Jung, K. Singh, E. S. Oh, J.S. Chung, 2013, *J. Power Sources*, *244*, 280.

42 M. C. Hsiao, C. Y. Chang, L. J. Niu, F. Bai, L. J. Li, H. H. Shen, J. Y. Lin, T. W. Lin, 2017, *Journal of Power Sources*, **345**, 156.

43 H. Li, R.Y. Tay, S.H. Tsang, W. Liu, E.H.T Teo, 2015, *Electrochim. Acta*, **166**, 197-205.

44 M.Saraf , K. Natarajan, S.M. Mobin, 2018. *ACS Appl. Mater. Interfaces*, **10**,16588.

45 G. Yu, L. Hu, M. Vosgueritchian, H.Wang, X. Xie, J.R. McDonough, X. Cui, Y. Cui, Z.

View Article Online
DOI: 10.1039/D0NA00021C

Bao, 2011, *Nano Lett,* 11,2905.

46 M. Karnan K. Subramani, N. Sudhan, N. Ilayaraja, M. Sathish, 2016, *ACS Appl. Mater. Interfaces*, **8**,35191.

47 W. Xiao, W. Zhou, T. Feng, Y. Zhang, H. Liu, L. Tian, 2016, *Materials*, **9**,783.

48 A.P. Alegaonkar, A.Kumar, S.H. Patil, K.R. Patil, S.K. Pardeshi, P.S.Alegaonkar,2013. *J. Phys. Chem. C,* **117,** 27105.

49 A.P. Alegaonkar, M.A. Mahadadalkar, P.S. Alegaonkar, B.B. Kale, S.K. Pardeshi, 2018, *Electrochim. Acta*, **291**,225.

50 S. Saha, M. Jana, P. Khanra, P.Samanta, H.Koo, N.C. Murmu, T. Kuila, 2015, *ACS Appl. Mater. Interfaces*, **7**, 4211.

View Article Online
DOI: 10.1039/D0NA00021C

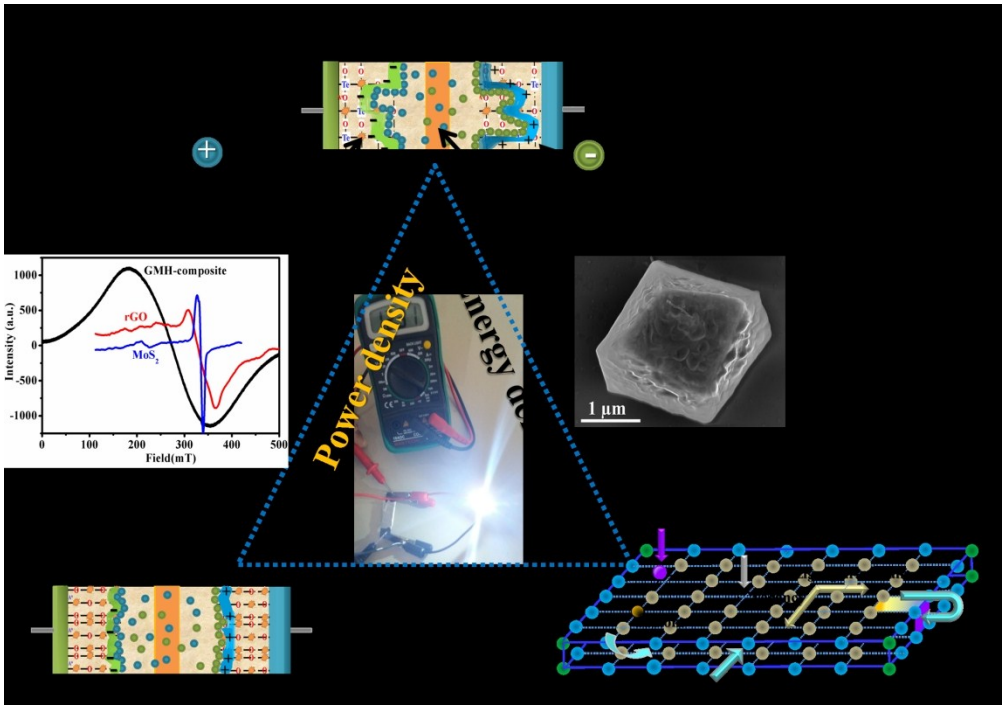

351x246mm (150 x 150 DPI)